JGR Earth Surface

RESEARCH ARTICLE
10.1029/2023JF007304

Active Seismic Refraction, Reflection, and Surface-Wave Surveys in Thick Debris-Covered Glacial Environments

Tyler Kuehn[1], John W. Holt[1,2], Roy Johnson[1], and Tyler Meng[2]

[1]Department of Geosciences, University of Arizona, Tucson, AZ, USA, [2]Lunar and Planetary Laboratory, University of Arizona, Tucson, AZ, USA

Key Points:

- We use ultra-dense receiver spacing to image a seismic reflection from the bottom of the loose debris layer on a debris-covered glacier
- We demonstrate that we can obtain the shear-wave velocity structure (stiffness) observations for debris cover on glaciers

Correspondence to:

T. Kuehn,
tkuehn@arizona.edu

Citation:

Kuehn, T., Holt, J. W., Johnson, R., & Meng, T. (2024). Active seismic refraction, reflection, and surface-wave surveys in thick debris-covered glacial environments. *Journal of Geophysical Research: Earth Surface*, *129*, e2023JF007304. https://doi.org/10.1029/2023JF007304

Received 22 JUN 2023
Accepted 18 DEC 2023

Author Contributions:

Conceptualization: John W. Holt, Roy Johnson
Data curation: Tyler Kuehn
Formal analysis: Tyler Kuehn, Tyler Meng
Funding acquisition: John W. Holt
Investigation: Tyler Kuehn, Tyler Meng
Methodology: Tyler Kuehn, John W. Holt, Roy Johnson, Tyler Meng
Project Administration: John W. Holt, Roy Johnson
Resources: John W. Holt
Software: Tyler Kuehn, Tyler Meng
Supervision: John W. Holt, Roy Johnson
Validation: Tyler Kuehn, Roy Johnson
Writing – original draft: Tyler Kuehn, Tyler Meng
Writing – review & editing: Tyler Kuehn, John W. Holt, Roy Johnson, Tyler Meng

Abstract Debris-covered glaciers (DCG) and rock glaciers have been increasingly studied in recent years because of the role they play within local watersheds, glacial ablation models due to climate change, and as analogs for buried ice features on planetary bodies such as Mars. Characterizing the supraglacial debris layer is a large part of these efforts. Geophysical exploration of DCG has mostly excluded active seismic methods, with the exception of refraction studies, due to the attenuating properties of the debris cover and field survey efficiency. We evaluate the accuracy, field efficiency, and effectiveness of seismic refraction, reflection, and surface-wave surveys for determining the elastic properties of the debris layer and any underlying layers on DCG using the Sourdough Rock Glacier in Southcentral Alaska as a test site. We provide evidence for imaging an ultra-shallow seismic reflection from the bottom of the loose debris layer using ultra-dense receiver arrays and compare it to ground-penetrating radar (GPR) images taken along the same profiles. We also detail how reliable dispersion curve images can be extracted from the surface wave package of the seismic data using the multi-channel analysis of surface waves technique, which allows for the (*s*)-wave profile to be inverted for. We find this could be a valuable addition to the toolbox of future geophysical investigations on DCG.

Plain Language Summary Debris-covered glaciers and rock glaciers are glaciers with a loose rock layer covering all or most of their surface. This layer can be several meters thick and plays an important role in how fast the glacier melts. These types of glaciers are an important analog to similar buried ice features observed on other planetary bodies, such as Mars. Typically, the subsurface of these glaciers is studied using the geophysical method of ground-penetrating radar (GPR), though in this paper we explore how active-source seismic methods could be utilized in future surveys. We demonstrate that using active-seismic techniques can provide information on the "stiffness" of the debris layer, which can add context to a GPR survey and ultimately aid in interpreting glacial features.

1. Introduction

Debris-covered glaciers (DCG) are unique geomorphological landforms that can be found across the globe anywhere clean-surfaced glaciers are formed, in high mountain environments where there is an abundant supply of rockfall debris. They are characterized by a surficial debris cover that varies in thickness spanning the accumulation zone to the glacier terminus. The debris layer acts as insulation for the subsurface ice, decreasing the ablation rate with increasing debris thickness (Östrem, 1959; see also Nicholson & Benn, 2006). The factors that contribute to the evolution of the debris surface and the physical properties within the debris are being increasingly studied in recent years to better understand the response of DCG to climate change (Rowan et al., 2015; Scherler et al., 2011; Yde & Paasche, 2010) and the effects on local watersheds, glacial hazards and landscape evolution.

In addition to these terrestrial applications, DCG has important planetary exploration implications for similar features observed on Mars (Head et al., 2010; Holt et al., 2008; Levy et al., 2014). Using DCG on Mars as a potential water resource for future exploration efforts and human habitation missions has been a recent topic in the planetary exploration community (Abbud-Madrid et al., 2016). The thickness of the debris layer, clast size distribution, and presence of ice-cemented debris are important parameters affecting the feasibility of in situ resource utilization that need to be accurately constrained in future planetary exploration studies.

Remote alpine environments and rugged terrain make exploration of DCG on Earth by drilling methods prohibitive in both cost and logistics to be widely used. For that reason, studies of the debris layer and internal structure of DCG have mostly relied on remote sensing data and geophysical exploration (Bhardwaj et al., 2014; Merz

et al., 2016; Paul et al., 2004). Among the suite of geophysical tools to study DCG, ground-penetrating radar (GPR) has been the most widely employed method for debris layer thickness investigations (e.g., Florentine et al., 2014; Petersen et al., 2020) because of the ease of use in rugged field settings and capability of imaging subsurface glacial structures.

In contrast, active seismic exploration methods have not been widely used on DCG with thick debris cover largely because of field efficiency issues and signal-to-noise ratios affected by the highly attenuating debris layer. Active-source seismic studies have been limited to (*p*)-wave refraction profiles and seismic refraction tomography (SRT), which have been shown to accurately delineate zones of pure ice from debris in ice-cored moraines and DCG (Croce & Milana, 2002; Langston et al., 2011; Musil et al., 2002; Potter, 1972) and have been combined with electrical resistivity methods (Pavoni et al., 2023; Wagner et al., 2019). Attempts at seismic reflection studies on rock glaciers have not been as successful (Maurer & Hauck, 2007; Musil et al., 2002).

The intent of this study is to apply and evaluate seismic reflection and active-source multi-channel analysis of surface waves (MASW) to quantify the thickness and elastic properties of the debris layer on rock glaciers. If appropriate acquisition parameters are followed, the data set for these surveys can be collected at the same time as a traditional SRT survey. To determine the effectiveness and accuracy of these methods, we compare the results of GPR profiles taken on coincident lines and synthetic seismic shot records using a finite-difference wave propagation modeler. We use results from refraction tomography profiles to inform the (*p*)-wave a priori values used in the reflection forward modeling and surface-wave inversion process. Our chosen study area is Sourdough Rock Glacier, located in the Wrangell mountains near McCarthy, Alaska. Previous GPR surveys have confirmed that the glacier features a debris layer approximately 2.5–3 m thick overlying an ice-rich core that extends up to 50 m in depth (Meng et al., 2022; Petersen et al., 2016).

2. Methods

2.1. Seismic Survey Methods

Seismic Refraction is a well-established tool in geophysical investigations for glaciology, where the start of the seismic signal, termed the (*p*)-wave first arrivals, is picked from the trace data. The result of the picking process is a set of times (*T*), usually in ms, and offsets from the source location distance (*X*), usually in m. The *T*-*X* information can then be inverted for the (*p*)-wave structure of the subsurface, and is useful for locating features such as bedrock, geological layer interfaces, or the water table. The depth of investigation depends on the velocity of the subsurface strata, the length of the seismic array, energy of the source, and attenuation properties of the materials (Musgrave, 1967).

Seismic reflection is a widely used method in oil and gas exploration and has also been used in glacial studies to determine glacier thickness and internal geometry (e.g., Baker et al., 2003). Reflections from the layer interfaces are returned to the receiver array as a hyperbolic event, due to a phenomenon called normal moveout (NMO). The NMO velocity can be solved by using the intercept time at zero offset and the geometry of the array (Dix, 1955). The records can then be corrected using the NMO for each reflection hyperbola event and stacked at a common depth point (CDP) to create an image of the subsurface layers (Sheriff & Geldart, 1982; Yilmaz, 2001).

Multi-channel analysis of surface waves (MASW) is a seismic exploration technique commonly used in civil engineering site characterizations. It is a useful tool to determine the (*s*)-wave properties of geology in the upper tens of meters of the subsurface when using an active source and dense receiver spacing (Park et al., 1999, 2007). The method takes advantage of the dispersive properties of Rayleigh waves, the main component of ground roll (Richart et al., 1970). The phase velocities at each frequency component of the Rayleigh waves can be used to yield a dispersion curve, which is inverted for a shear (*s*)-wave velocity profile of the subsurface (Park et al., 1999). In typical seismic refraction and reflection shot records, the ground roll resulting from the source can be seen as a distinct cone-shaped event propagating out from the source location. The ground roll is often unwanted and filtered out of the record to identify other events of interest such as reflections (Karslı & Bayrak, 2004; Yilmaz, 2001), but MASW acquisition parameters seek to enhance the ground roll. Since Rayleigh waves can be generated using a compressive source typically used for (*p*)-wave surveys, seismic refraction, reflection and MASW surveys can use the same data set, given that the time of the shot records is long enough to capture the whole ground-roll package at the farthest offset. The analysis assumes that the wavefront is propagating as a plane wave, so the source must be offset at a far enough distance from the first receiver to approximate the needed

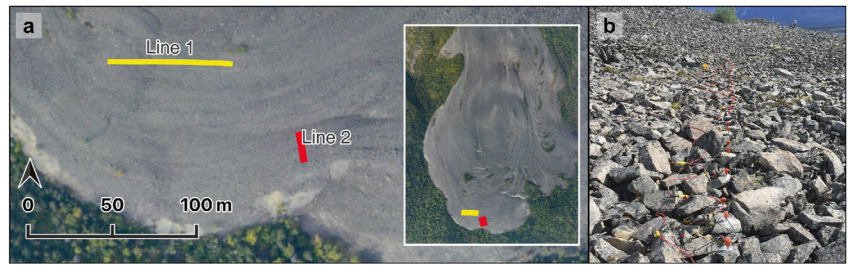

Figure 1. (a) Seismic line locations near the terminus of Sourdough Rock Glacier and inlay map for the full glacier context. (b) Field photo of typical terrain on Sourdough Rock Glacier with geophones ground-coupled for line 1 at 0.5-m intervals.

wavefront characteristics. High-frequency surface waves are also easily attenuated, so a maximum offset depending on site characteristics needs to be chosen as well (Park et al., 1999).

2.2. Survey Geometry

For a baseline comparison with the active seismic methods, we collected GPR profiles along the active seismic lines on Sourdough using a Sensors and Software PulseEKKO Ultrasystem operated with 200-MHz antennas. The antenna spacing was 0.5 m and traces recording received power as a function of time were collected at discrete 0.1-m intervals along the profile, allowing for the detection of the radio echo from the dielectric contrast between the debris and the ice.

For the active seismic measurements, two 24-channel Geometrics Geode seismographs using 40-Hz geophones were connected to create 48-channel linear arrays. The active seismic survey lines were chosen near the terminus of the glacier over relatively flat areas of the debris surface. Line 1 is oriented roughly east-west with a spacing of 0.5 m. Five overlapping sub-arrays of lengths of 24 m created a total transect length of 72 m. Line 2 is oriented roughly north-south with a total of 48 receiver stations spaced 0.3-m apart that span a total distance of 14.4 m (Figure 1). We used a recording sampling rate of 0.063 ms. At Line 1, five shots were repeated at each source point to enhance the signal to noise ratio. For line 2, 10 shots per source point were collected.

2.3. Seismic Source and Receivers

The purpose of using 40-Hz frequency geophones on Sourdough was primarily to collect shallow reflection data at high frequencies (Brabham et al., 2005; Steeples et al., 1997), though we also use the data set for MASW. A study by Park et al. (2002) detailed the use of higher-frequency geophones for MASW and found that a reliable dispersion curve was still attainable and the receivers were able to record at frequencies lower than 10 Hz, though it does limit the investigation depth depending on site characteristics. Since the aim of our surface-wave study was the upper few meters of the subsurface, we found this acceptable in order to simultaneously carry out a reflection survey.

To couple the receivers to the debris surface, geophones with spikes were placed in 0.95 cm (⅜ inch) diameter holes that were drilled into debris clasts using a cordless hammer drill (Figure 2). This method of coupling was chosen because it allowed for precise positioning of geophones on the survey line and allowed for the minimization of geophone tilt (Maurer & Hauck, 2007). Each receiver was geo-located using a multi-band RTK GNSS receiver with centimeter precision at the top of the geophone. The approximate height at which each geophone sits above the surface, 9 cm, was subtracted from the elevation values at each station to infer a topography profile for the top of the debris layer.

A 7.25 kg (16-lb) sledgehammer and a standard 0.63 kg (22 oz) geologist's rock hammer were used as sources during acquisition. The varying shape and size of the surface debris on Sourdough ruled out the possibility of using a steel plate as an impact surface for the source because of inadequate coupling, resulting in the plate bouncing after being struck. Since using an impact surface was not possible, the source was struck directly on debris-clasts at each shot point. Most of the surface rocks are loose and platy, which resulted in debris movement, breakage, and flyrock after sledgehammer strikes, producing unwanted events in shot records. During the acquisition, shot records with obvious effects from these events were not kept after visual inspection.

Figure 2. Method for geophone coupling to individual debris clasts after Maurer and Hauck (2007).

After some time in the field, it became evident that shots recorded with the rock-hammer source yielded better field efficiency, less source-generated noise, and more shots could be stacked at a particular shot location. For those reasons, only the rock hammer was used for reflection acquisition on the last half of the Line 1 and the whole of Line 2, with shot locations at every receiver station. The heavy sledgehammer was then used at either end of the arrays to generate forward and reverse shots used for MASW, because the observed surface-waves were stronger than those generated by the rock hammer.

3. Processing

3.1. GPR

Using Sensors and Software EKKO_Project software, we subtracted the background average, migrated the data, and applied a depth correction assuming a velocity of 0.1 m/ns, which corresponds to a dielectric permittivity of nine. This value is consistent with debris values from GPR studies on other DCGs (Meng et al., 2022; Monnier & Kinnard, 2013; Petersen et al., 2020) and provides a lower bound on estimated debris thickness because most lithologies do not have a dielectric permittivity exceeding nine (Campbell & Ulrichs, 1969). By picking the first break of the reflection interpreted to be the debris/ice interface, we find a minimum debris thickness of 1.5 m and a maximum debris thickness of 2.2 m along these transects. A comparison of the GPR results and final seismic reflection processing results can be seen in Figure 10. The uncertainty in the dielectric permittivity of the debris is the largest source of uncertainty in the GPR-derived debris thickness measurements.

3.2. SRT First Break Picking

To pick the first arrival times, we normalize the shot traces and manually pick the break times. In the shot records, the *p*-wave first arrivals (the seismic wave traveling along the surface of the debris) are obscured by the air wave (sound of the hammer hitting the surface) at short offsets (0–5 m) (Figure 3). In these records, the airwave has a much higher frequency content and lower amplitude than the first arrivals, so the two can be distinguished to pick a reliable first arrival time for the debris layer. Records that had high amounts of source-generated noise were avoided and clean records were used for the tomography inversion.

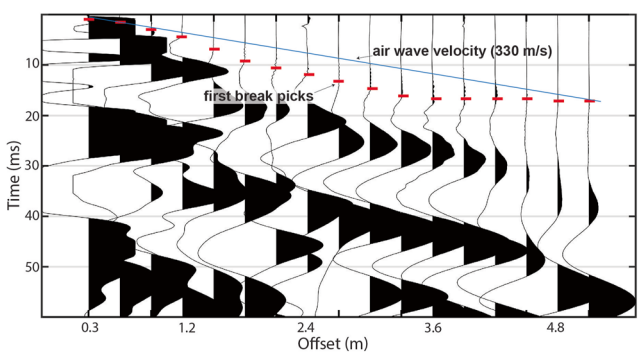

Figure 3. An example shot record from Line 2 for near-offset receivers. The first arrival *p*-wave (red dashes) is obscured by the air, which is represented by the line having a slope of 330 m/s and recognized by high-frequency low-amplitude arrivals.

3.3. Reflection Processing

For reflection processing, individual shot records taken at each station were stacked by source location and elevation statics were applied using the replacement velocity of 185 m/s observed from the first *p*-wave arrival times to account for the elevation differences between the receivers. Spectral analysis of the individual stacked records shows relatively low frequencies (Figure 4) for both lines although the frequency response of Line 2 returns higher frequencies than Line 1 due to the smaller receiver spacing and smaller total array length of the line. However, the majority of the recorded

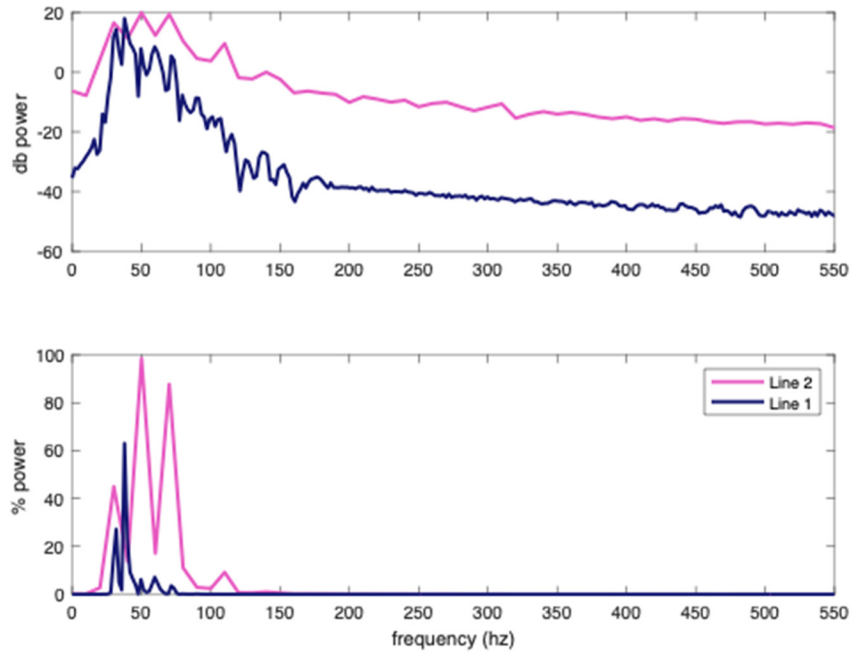

Figure 4. Frequency content of the recorded signal from an example record from Line 1 (0.5 m receiver spacing, total length = 24 m) and Line 2 (0.3 m receiver spacing, total length = 14.4 m).

frequencies occur below 100 Hz and visual inspection of the stacked shot records and CDP gathers at high frequencies confirms that no reflections can be identified when filtering for frequencies above this value for both lines.

Using a bandpass filter with corner values at 16–24 to 140–180 Hz, a reflection hyperbola can be picked around 21 ms in the high-fold CDP gathers for Line 1 and around 22 ms for Line 2, both characterized by a normal move-out velocity of 185 ± 15 m/s (Figure 5), which becomes asymptotic to the direct wave. Implementation of a minimum-phase spiking deconvolution filter with a white noise level of 0.1 was found to increase the resolution of this event and decrease the associated multiple energy. Additional processing steps included surgical muting to eliminate ground roll and direct-wave energy. Automatic gain control was also applied.

3.4. Synthetic Seismic Generation

We assign layer properties used for the reflection forward modeling and as a priori values for the inversion of the surface-wave data using observed values from the observed first arrivals and studies on other glaciers cited in Table 1. The table is a simple four-layer model interpretation of the overall glacier structure and does not consider internal variations of compaction within the debris layer, the likely presence of partially ice-cemented debris near the surface, or internal debris in the glacier core.

To accurately interpret and pick reflection hyperbola in the Sourdough field records, we generate synthetic shot records based on expected velocity structures for both lines. To do this, we use the finite-difference wave propagation modeler SPECFEM-2D (Komatitsch, 1997; Komatitsch et al., 1998; Xie et al., 2014) and the layer properties defined in Table 1 to generate the models depicted in Figure 6. The synthetics generated from these models used the same receiver geometry as our field data. Model 1 and Model 2 are simplified representations of the expected structure based on the GPR results and the observed and expected seismic velocities from Table 1. Model 3 exaggerates the ice thickness of Model 1 to see if a signal from the glacier bed influences the trace data. If a signal from the glacier bed influences the synthetic record for Model 1, we should observe a change for Model 3, as the bed response would occur at a much later time. The wave propagation parameters assume no attenuation factors. The center frequency of the source is evaluated at 100 Hz (the frequency of the observed first arrival wavelet in the field records shown in Figure 3) and 500 Hz, which allows for easier visual separation of refraction and reflection events (Figure 7).

It should be noted that while the synthetic models have a shear-wave velocity assigned to each layer, they do not accurately represent the complex shear-wave variations within the debris. Therefore, the ground-roll Rayleigh

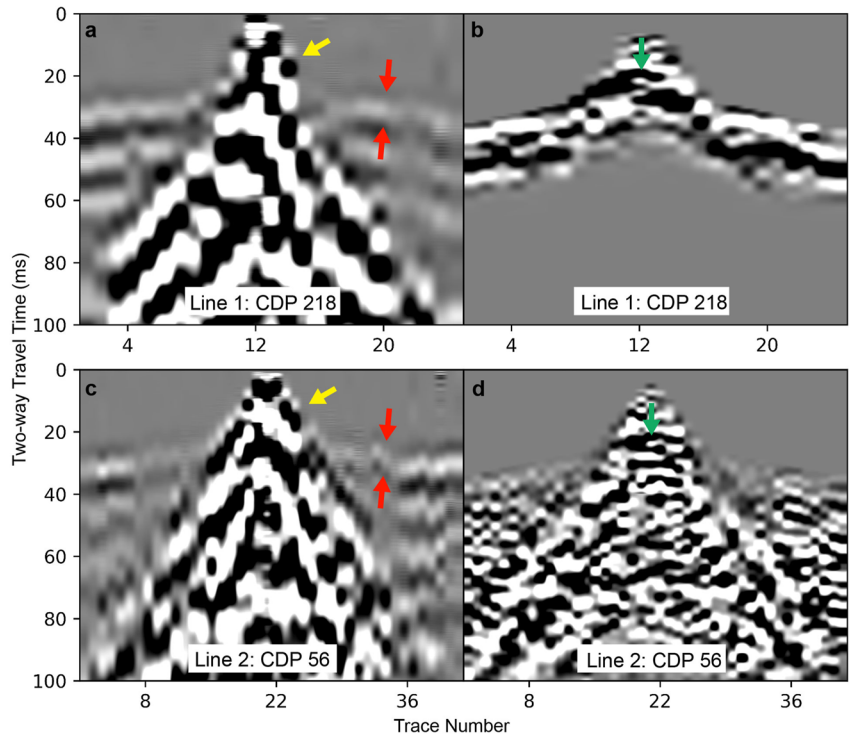

Figure 5. (a) Raw common depth point (CDP) gather for Line 1 CDP bin #218 with the direct wave denoted by the yellow arrow and the refraction first-arrival wavelet denoted between the two red arrows. (b) After processing and muting the first-arrival energy. (c) Raw CDP gather for Line 2 CDP bin #56 with the same notation as (a). (d) After processing and muting the first-arrival energy. A weak reflection hyperbola indicated by the green arrows can be picked in (b) and (d) with a normal move-out velocity of 185 ± 15 m/s. The SEGYIO python software was used to generate the figure.

waves are not adequately duplicated in the synthetics and an analogous surface-wave package cannot be picked. Due to this limitation, we use the synthetic shot records as a comparison for potential reflection events only and not for a synthetic comparison to the field surface-wave data in the MASW inversion process.

3.5. MASW Dispersion Curve Extraction

Preliminary MASW processing included stacking multiple individual shot records by source location and applying a surgical mute to isolate the surface waves. The complex velocity structure of the debris layer on Sourdough necessitates custom muting for each stacked shot record to accurately isolate the surface waves, instead of general

Table 1
Sourdough Rock Glacier Layer Properties for the Loose Debris (L_1), Interpreted Ice-Cemented Debris (L_2), Ice-Rich Core (L_3), and Bedrock (L_4) Using the Observed Refraction Data and Values From the Literature

	V_p (m/s)	ρ (g/cm^3)	h (m)	Notes
L_1	185 ± 15*	1.85 ± 0.1†	1.5–2.5	*Slope of direct-wave first arrivals; †Calculated using debris clast density of 2.65 g/cm^3 and estimated layer porosity of 0.3 (Anderson & Anderson, 2018) and the bulk density equation[a]
L_2	1,600 ± 400*	1.6 ± 0.1†	1–2	*From observed data; †Average density of permafrost (Kawasaki et al., 1983)
L_3	3,650 ± 150*	0.95 ± 0.05†	12–30	*Clean glacial ice velocity from observed data and previous studies (Kohnen, 1974; Press, 1966); †Density of glacial ice (Shumskiy, 1960)
L_4	4,800*	2.65†		*,†Meta-sedimentary bedrock estimations (Press, 1966)

Note. A range of observed thicknesses (h) from the refraction data and ground-penetrating radar measurements.
[a]$\rho_b = (1 - f)\rho_s$ where ρ_b is the bulk density, f is the porosity, and ρ_s is the particle density.

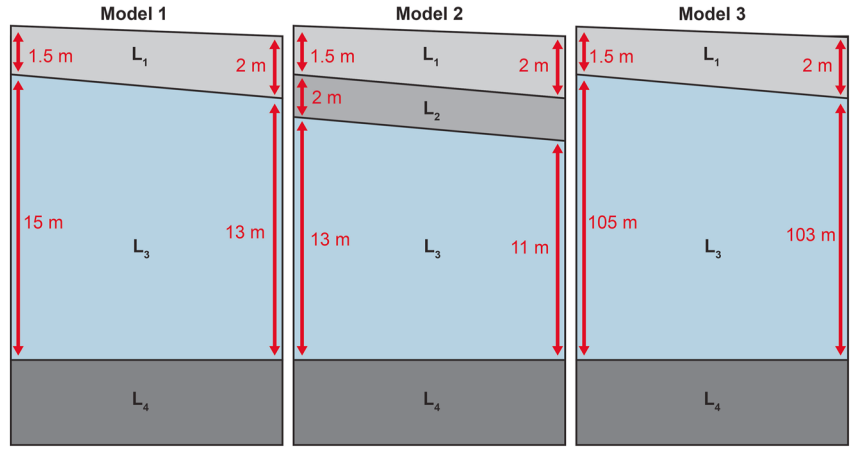

Figure 6. Representation of the simplified glacier structures used in the synthetic forward modeling of Sourdough Line 2. The (p)-wave and density values for the corresponding layers are listed in Table 1. The geometry of the loose debris layer (L_1) and ice-cemented debris layers (L_2) are from the ground-penetrating radar and refraction tomography observations. The length along the model corresponds to the array length of Line 2, which we use to compare the synthetic results against the field records in Figure 7.

mutes based on offset for all records. A bandpass filter with corner frequencies of 2–4 to 50–80 Hz was also applied.

A minimum offset of 5.5 m was used when selecting traces for the analysis to account for the near-field effects of non-planar wave propagation. After visual analysis of dispersion-image coherence, it was determined that a maximum offset of 18 m could be used for trace selection. Incorporating traces at larger offsets greatly reduced the quality of the dispersion image.

To extract the experimental dispersion curve from the shot records, the MASWaves software (Olafsdottir et al., 2018) was used. MASWaves applies a Fourier transform to the trace data, normalizing for each phase velocity and wavelength set and summing the set amplitudes to create a dispersion image (Figure 10). The experimental dispersion curve was then manually picked from the peak values of the dispersion image. We then inverted the picked fundamental mode of the dispersion curve to yield a 1-dimensional shear-wave (V_s) velocity profile in the MASWaves software. A limitation of MASWaves is that higher modes of the dispersion image are not able to be accounted for in the inversion process. A multi-modal inversion process could lead to more accurate results and a larger depth of investigation.

4. Results

4.1. SRT

To invert the refraction data, we use the python Geophysical Inversion Modeling Library (Rücker et al., 2017), which uses a shortest-path algorithm (Heincke et al., 2010; Ronczka et al., 2017) to calculate seismic ray paths from the modeled velocity structure. The inversion scheme requires a data weight for each travel-time pick, which we assign as a linear function based on source-receiver offset used in other shallow refraction tomography studies, where error increases with offset (Flinchum et al., 2022), in this case a minimum of 1 ms and a maximum of 3 ms. The values of these errors were assigned based on the standard deviation from the mean pick time of a representative shot record for close and far offsets.

For interpretation of the inversions, we compare the results to previously described seismic velocities in glacial and permafrost environments. Glacial ice has a typical (p)-wave velocity range of 3,600–4,000 m/s (Baker et al., 2003; Press, 1966) when free of any entrained debris and frozen soils can have a (p)-wave velocity range from 2,400 to 3,200 m/s (Leblanc et al., 2011). Dry or well-drained sediments or gravels have an expected range of 100–800 m/s (Press, 1966; Uyanık, 2011).

For the Sourdough lines, after 15 iterations we achieve a χ^2 value of 1.12 and an RMS of 1.02 ms for line 1 and a χ^2 value of 0.469 and an RMS of 1.848 ms for line 2 (Figure 9). The loose debris layer ranging from 1.5 to 2.5 m

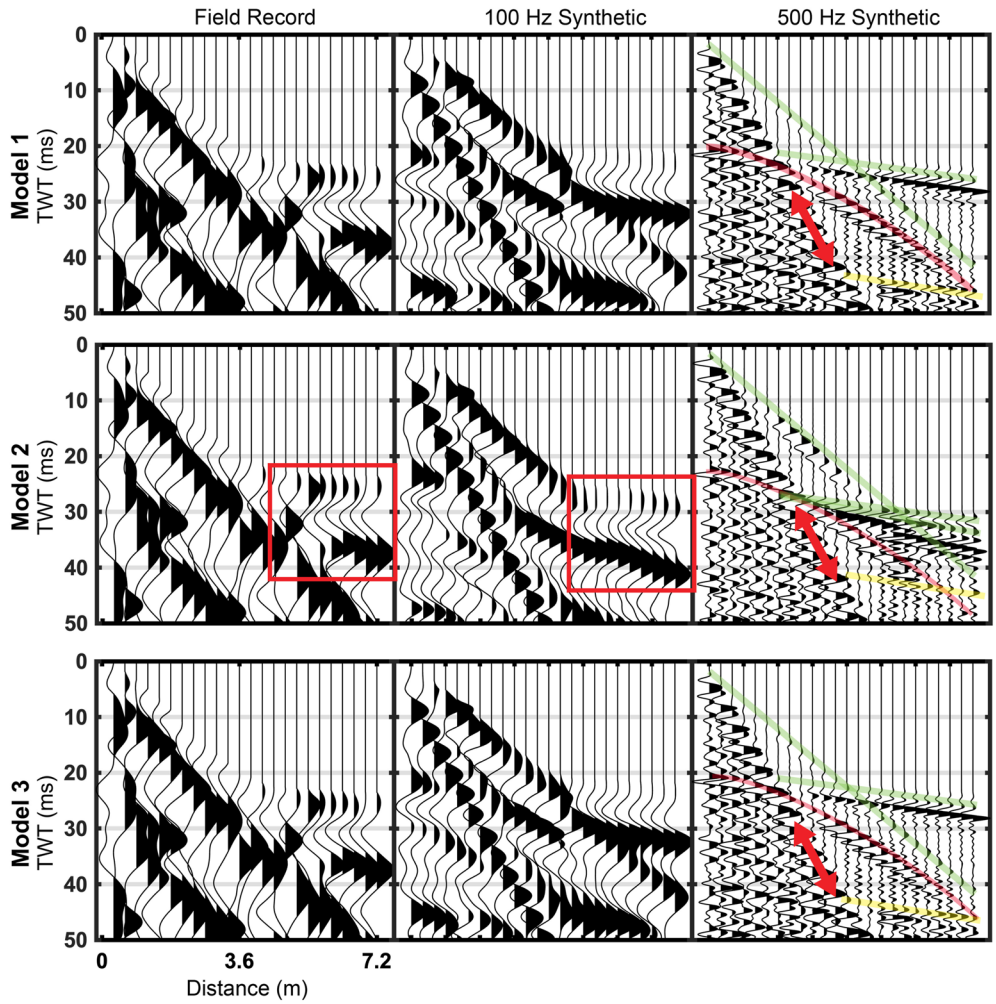

Figure 7. Line 2 Field record (ffid 3,255) and synthetic record comparison of model 1 (top), model 2 (middle), and model 3 (bottom) parameters. The direct wave and refraction events are highlighted in green, the bottom of the debris layer reflection hyperbola in red, and the refraction multiple in yellow. The red double-sided arrow marks the strong surface wave event in the debris layer that does not match the field data. The better visual match between the Model 2 far-offset events and the field data is outlined by the red boxes.

depth is characterized by a (*p*)-wave velocity around 185 m/s but shows increases toward 1,000 m/s toward the interface with the ice core.

4.2. Reflection Depth Sections

Figure 10 shows the stacked CDP depth sections for the Sourdough reflection surveys. The sections were migrated to depth sections using a velocity of 185 m/s picked from the reflection hyperbolas in the CDPs discussed earlier. The first half of the Line 1, for which the source was a 16-lb sledgehammer, yields no reliable reflector and is not imaged in the final results. The lack of a reflector for this portion of the line is probably a result of the signal-to-noise ratio, with much more source-generated noise associated with shots taken with the sledgehammer versus the rock hammer. The last half of the Line 1 from meters 37 to 72, where the rock hammer was used as a source, yielded better results. The imaged reflector is interpreted as the bottom of the loose debris layer and agrees with the reflector picked from the coincident GPR data. The closer receiver spacing for Line 2 yields a stronger reflector from the bottom of the loose debris layer and lateral variability of the interface depth is more apparent. Comparing the seismic reflection results to the GPR results (Figure 7), it is apparent that the GPR yields more coherent data, as there is a higher signal to noise ratio than the seismic data. It is encouraging that the picked seismic reflection for the bottom of the loose debris closely matches the behavior of the interpreted reflection from the GPR data.

4.3. MASW Inversion

Figure 11 displays the inversion for an example record. The inversion scheme in MASWaves is an iterative trial-and-error forward modeling comparison. For our inversions, the V_p parameter was fixed while we varied the V_s and density parameters. Here we display the results from the parameters which best fit the observed data curve in the upper 3.5 m and change the half-space parameters to see if the data are being influenced by waves traveling in an ice-rich layer. The best-fitting Model 1 parameters are analogous to ice-cemented debris half-space starting at 2.5 m depth and Model 2 adds parameters analogous to an ice-rich half-space at 3.5 m depth. The NRMSE for Model 1 is 5.7% and the NRMSE for Model 2 is 8.5%. From these errors, it can be concluded that any surface waves being generated in the ice-rich core are not affecting our observed fundamental mode. As we noted earlier, a full-waveform analysis and multi-modal inversion scheme could provide a higher depth of investigation.

5. Discussion

5.1. SRT

Our observed velocity for the very shallow debris layer (0–1 m depth) differs significantly from previous refraction studies done on DCG, where velocities around 500 m/s have been observed for the debris mantle (Bucki et al., 2004; Pavoni et al., 2023), though 300 m/s has been observed as well (de Pasquale et al., 2022). Our study differs from the ones noted here in the receiver spacing, where the other studies used 3–15 m, whereas we used 0.5 and 0.3 m, allowing us to characterize the debris layer velocity as gradational and highly variable. The observed 185 m/s direct wave velocity at near offsets is a function of the complicated path the direct arrival has to take to the geophones. The cobbles that make up the debris most likely have a *p*-wave velocity in the range of granitic rocks (5,000–6,500 m/s), but the odd coupling between cobbles and the large void space between them complicates the path the direct wave has to take to the receivers.

The depths of the modeled velocities agree with the interfaces indicated by the GPR profiles (Figure 10). A thin layer beneath the loose debris with velocity values between the loose debris and pure ice values is interpreted as an ice-cemented debris-layer. Velocities approaching near pure-ice values are modeled starting at 3.5 m depth for Line 1 and 4.5 m for Line 2. The modeled ray paths for Line 2 extend deeper than those for Line 1, even though the array length is shorter. This could be due to discontinuous ice-rich zones and a thicker ice-cemented debris layer, which would not provide a sharp layer interface for the refracted wave to travel along, as observed for Line 1.

5.2. Reflection

No reflection hyperbolae were visually detectable at later times associated with deeper interfaces, such as an ice-cemented debris layer or the glacier bed. Figure 7 compares the results from the synthetic shot records to the field data. Our recorded frequencies show that no discernible reflections can be picked in the unstacked field records, which we replicate in the 100 Hz synthetics. The synthetic models at 100 Hz visually match the observed data fairly well, though Model 2 produces a better match for the farther-offset events noted by the red boxes, possibly due to the presence of a thin ice-cemented debris layer. There are differences in the first arrivals between the synthetics and field data, a result of the non-planarity of the layer interfaces and lateral changes in the dip angle, which we could not capture. However, the simplified synthetic structure provides a general analog to the field data.

The lack of an observed bed reflector in the synthetic models can be explained by the reflection and transmission coefficients of the debris-ice interface (Sheriff & Geldart, 1982). Reflection and transmission coefficients are strongly affected by the difference in acoustic impedance (a product of layer density and seismic velocity) of each geologic layer. Table 2 lists the reflection coefficients for Models 1 and 2 at normal-incidence of a pure-elastic medium using the layer properties from Table 1. In both models, the debris layer has a very strong reflection coefficient (Model 1 $R_{mean} = 0.81$; Model 2 $R_{mean} = 0.749$), which prevents source energy from transmitting to deeper layers as well as the transmitted energy from returning to the surface, which is below 5% for both models. These calculations do not include attenuation effects from scattering, geometrical spreading, or non-normal incidence, which would decrease the amount of returned energy even further. This could explain why a deeper reflector

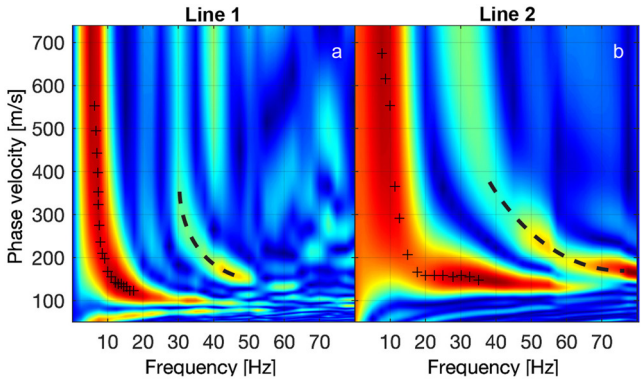

Figure 8. Examples of normalized amplitude dispersion spectrum images from Sourdough Line 1 (a) and Line 2 (b). The picked fundamental mode of the dispersion curve is marked with black crosses and identified strong first higher modes as dashed black lines.

like the one marked by the yellow arrows in the radar profile (Figure 2) or a glacier-bed reflection does not appear in the individual seismic shot records or CDP gathers.

5.3. MASW

Examples from Sourdough indicate that with a close receiver spacing and source offset limited to a maximum of 18 m, a reliable and clean dispersion curve can be extracted from the surface-wave package. The Sourdough curves display strong frequency amplitude below 10 Hz (Figure 8) even with 40-Hz geophones. The curve for Line 2 is smoother compared to Line 1, indicating that closer receiver spacing leads to a more defined curve, although this could also be due to differences in the velocity structure, as the debris cover is a laterally complex medium.

Sourdough Model 1 (Figure 11) indicates that the surface waves are very sensitive to the complex velocity structure within the debris and ice-cemented debris layers. The five-layer model shows that the debris layer can be characterized by an (*s*)-wave range of 30–160 m/s. The model supports an increase to an (*s*)-wave velocity of 680 m/s at 2.5 m depth, which is below the typical permafrost (*s*)-wave range of 1,000–1,650 m/s and massive ice range of 1,550–2,050 m/s (Killingbeck et al., 2018; Press, 1966; Tsoflias et al., 2008; Yang et al., 2011). This could indicate that at 2.5-m depth there is some ice-cementation but voids or melt could also be present. This supports the previously discussed observations that the debris layer on Sourdough is highly variable laterally but ultimately gets more consolidated with depth.

6. Conclusions

The primary goal of this study was to image the shallow debris-ice interface of DCG using active seismic methods and to yield more useful information from the seismic record than just the refraction first arrivals. Previous exploration studies using active seismic methods have so far been limited to refraction analysis, but we demonstrate that ultra-dense arrays generate more high-quality information for extraction from the seismic shot records, and the methods can be useful for characterizing the elastic parameters of the very shallow subsurface of these glaciers.

While we are able to image a reflection from the survey on Sourdough, it is apparent that GPR methods can provide more reliable and precise reflection measurements due to the frequencies involved and the higher signal to noise ratio of the acquired data, allowing it to have the ability to image the deeper reflections in the subsurface on these glacial features. The shortfalls of the GPR method are the uncertainty in the dielectric permittivity of the debris and an assumed velocity for the whole section. In this regard, seismic methods can provide insight as the velocities are observed from the data, which reduces uncertainty in the interpretation. We were able to image a reflection from the bottom of the loose debris layer, which was the primary goal of the reflection work on Sourdough. Secondary goals of imaging deeper reflections were not successful, which we explain by the fundamental acoustic properties of the velocity structure and synthetic record comparison. We observe that high-frequency filtering, typically above 400 Hz for ultra-shallow reflection processing (Steeples & Miller, 1998), is not possible with reflection data collected on DCG of this nature due to the highly attenuating properties of the debris layer. Most of the recorded frequency values occur in the 20–60 Hz range and no coherent signals appear in the individual shot records or CDP gathers when looking at high frequency-filtering windows.

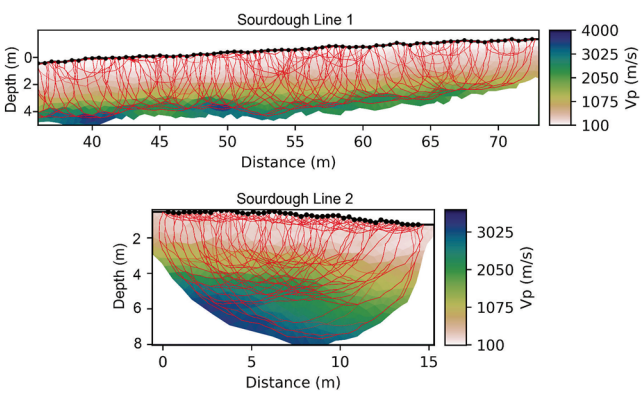

Figure 9. Results from the refraction tomography inversions for Line 1 (top) and Line 2 (bottom). Modeled ray paths are drawn in red, with paths associated with multiple rays brighter than paths associated with fewer rays. Receiver locations are shown as black dots.

We demonstrate that a reliable and clear dispersion curve can be extracted from the surface wave package of the seismic shot records if dense receiver spacing and appropriate near and far offsets are used. We are able to obtain a 1D V_s profile for these records, which fall within our expectations for the

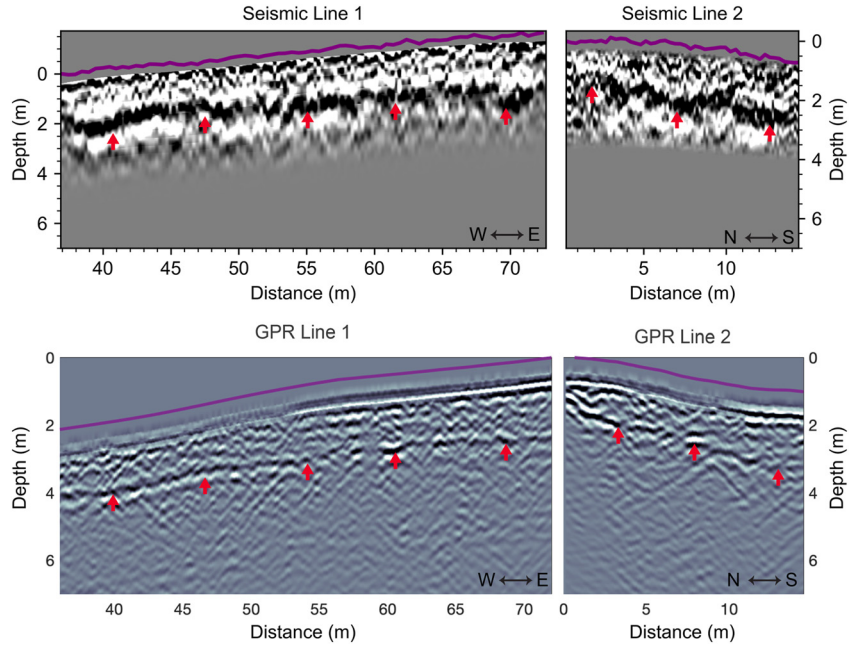

Figure 10. (top) Seismic Line 1 and Seismic Line 2 processed and stacked common depth point sections from the Sourdough glacier reflection surveys converted to depth. The reflector denoted by the red arrows is interpreted to be the bottom of the loose debris. The purple line indicates the approximate topography of the debris surface from GPS data collected at each receiver station and corrected for geophone height. Depth = 0 is relative to the surface at the first receiver station in each line. (bottom) The ground-penetrating radar (GPR) results are corrected for topography and displayed for comparison, with the red arrows denoting the bottom of the loose debris. Differences in the topography line are a result of using a Topcon SGR-1 DGPS for the PulseEKKO GPR system and a RTK GNSS receiver for the seismic geophone locations, which is described in Section 2.2.

debris layer using only the fundamental mode of the dispersion curve. Future surveys could not only image this in 2D or 3D depending on the array but also invert identified higher modes of the dispersion curve to get a deeper profile. When combined with electrical resistivity surveys, void space, melt zones in the debris layer, snow compaction within the debris and debris entrainment within the ice could be interpreted.

To achieve a field efficiency closer to GPR acquisition, future surveys investigating the shallow structure of DCG could be designed using distributed acoustic sensing (DAS). As we have shown, results can be achieved with very small receiver spacings, which makes DAS a logical next step since measurements can be recorded at any

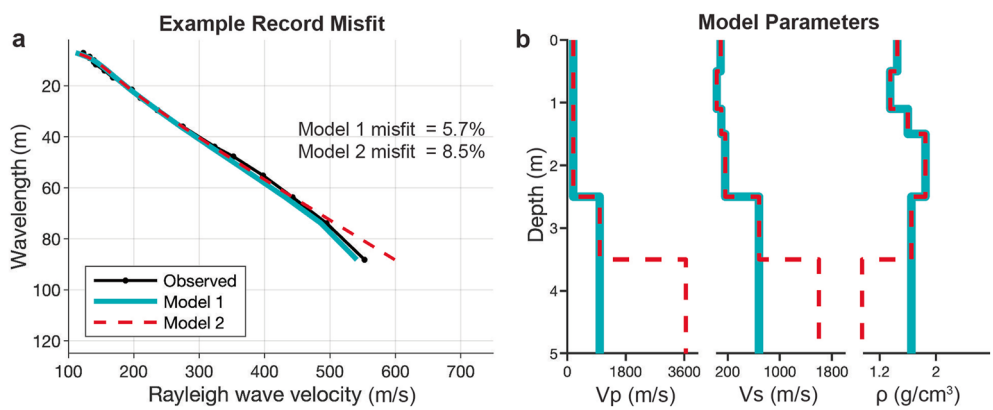

Figure 11. Results of the fundamental-mode inversion process for V_s models analogous to an ice-rich halfspace (red dashed line) and an ice-cemented debris halfspace (blue). The observed dispersion curve is plotted in black in (a) against the models. The forward model input parameters V_p, V_s, and ρ are plotted in (b).

Table 2
Reflection (R_{mean}) and Transmission (T_{mean}) Coefficients at Normal-Incidence to the Source for the Pure-Elastic Simplified Velocity Structures Modeled in the Synthetic Shot Records (Figure 6) Using the Zoeppritz Equations (Sheriff & Geldart, 1982)

Layer properties	Interface	R_{mean}; T_{mean}	Coefficient range	% Returned to surface
Model 1 and model 3 layer parameters				
$L_1 = V_{p1}$ (185 ± 15); ρ_1 (1.85 ± 0.1)	L_1/L_2	0.81; 0.19	±0.03	81 ± 3%
$L_2 = V_{p2}$ (3,650 ± 150); ρ_2 (0.95 ± 0.05)				
$L_3 = V_{p3}$ (4,800); ρ_3 (2.65)	L_2/L_3	0.552; 0.448	±0.033	2.2 ± 0.77%
Model 2 layer parameters				
$L_1 = V_{p1}$ (185 ± 15); ρ_1 (1.85 ± 0.1)	L_1/L_2	0.749; 0.251	±0.07	74.9 ± 7%
$L_2 = V_{p2}$ (1,600 ± 400); ρ_2 (1.6 ± 0.1)	L_2/L_3	0.162; 0.838	±0.148	1.62 ± 1.58%
$L_3 = V_{p3}$ (3,650 ± 150); ρ_3 (0.95 ± 0.05)				
$L_4 = V_{p4}$ (4,800); ρ_4 (2.65)	L_3/L_4	0.552; 0.448	±0.033	3.6 ± 2.4%

Note. (p)-wave velocities are in m/s and densities in g/cm^3. The amount of source energy returned to the surface is very high for the bottom of the debris layer and negligible before attenuation effects from deeper layers.

point along the fiber optic cable. DAS uses Rayleigh backscattering from a laser impulse to record vibrations or changes along a fiber optic cable (Kingsley, 1986) generated by a source at any point along the cable. While field efficiency for active seismic DAS surveys would be much greater than setting up a traditional geophone array like this survey uses, further work to understand the coupling between a DAS cable and the debris surface would need to be examined, although preliminary work (Spikes et al., 2019) indicates that coupling of fiber optic cables would be sufficient for such investigations.

The observations from this study fill in some gaps for seismic velocity observations on debris-covered glacial surfaces. We provide evidence that if proper acquisition and processing parameters are observed, more information than just the seismic first arrivals can be extracted from the data and the uncertainty in the interpretation of these features can be reduced.

Data Availability Statement

The SEG-Y shot record data for the Sourdough glacier acquisition are archived under seismic network code 2E_2021 at the IRIS PASSCAL DMC and can be requested using dataset report number 22-003 (Holt, 2021). The GIS data collected for each site, GPR data in segy format, parameter files for the SPECFEM2D modeling, and example scripts for the refraction tomography, MASW and reflection image plotting are available at (Kuehn, 2023) https://doi.org/10.25422/azu.data.19758499.

Acknowledgments
This work was funded by The University of Arizona and National Science Foundation Grant 1929577. We thank Stefano Nerozzi, Michael Christoffersen, and Victor Devaux-Chupin for their assistance in the field data acquisition. We also thank Brady Flinchum of Clemson University for advice and modification of his pyGiMLI scripts.

References

Abbud-Madrid, A., Beaty, D., Boucher, D., Bussey, B., Davis, R., Gertsch, L., et al. (2016). Mars water in-situ resource utilization (ISRU) planning (M-WIP) study. Retrieved from https://www.researchgate.net/publication/301614744_Mars_Water_In-Situ_Resource_Utilization_ISRU_Planning_M-WIP_Study

Anderson, L. S., & Anderson, R. S. (2018). Debris thickness patterns on debris-covered glaciers. *Geomorphology*, *311*, 1–12. https://doi.org/10.1016/j.geomorph.2018.03.014

Baker, G. S., Strasser, J. C., Evenson, E. B., Lawson, D. E., Pyke, K., & Bigl, R. A. (2003). Near-surface seismic reflection profiling of the Matanuska Glacier, Alaska. *Geophysics*, *68*(1), 147–156. https://doi.org/10.1190/1.1543202

Bhardwaj, A., Joshi, P. K., Singh, M. K., Sam, L., & Gupta, R. D. (2014). Mapping debris-covered glaciers and identifying factors affecting the accuracy. *Cold Regions Science and Technology*, *106–107*, 161–174. https://doi.org/10.1016/j.coldregions.2014.07.006

Brabham, P. J., Thomas, J., & McDonald, R. J. (2005). The terrestrial shallow seismic reflection technique applied to the characterization and assessment of shallow sedimentary environments. *Quarterly Journal of Engineering Geology and Hydrogeology*, *38*(1), 23–38. https://doi.org/10.1144/1470-9236/04-033

Bucki, A., Echelmeyer, K., & MacInnes, S. (2004). The thickness and internal structure of Fireweed rock glacier, Alaska, U.S.A., as determined by geophysical methods. *Journal of Glaciology*, *50*(168), 67–75. https://doi.org/10.3189/172756504781830196

Campbell, M. J., & Ulrichs, J. (1969). Electrical properties of rocks and their significance for lunar radar observations. *Journal of Geophysical Research*, *74*(25), 5867–5881. https://doi.org/10.1029/JB074i025p05867

Croce, F. A., & Milana, J. P. (2002). Internal structure and behaviour of a rock glacier in the Arid Andes of Argentina. *Permafrost and Periglacial Processes*, *13*(4), 289–299. https://doi.org/10.1002/ppp.431

de Pasquale, G., Valois, R., Schaffer, N., & MacDonell, S. (2022). Contrasting geophysical signatures of a relict and an intact Andean rock glacier. *The Cryosphere*, *16*(5), 1579–1596. https://doi.org/10.5194/tc-16-1579-2022

Dix, C. H. (1955). Seismic velocities from surface measurements. *Geophysics*, *20*(1), 68–86. https://doi.org/10.1190/1.1438126

Flinchum, B. A., Holbrook, W. S., & Carr, B. J. (2022). What do P-wave velocities tell us about the critical zone? *Frontiers in Water*, *3*, 772185. https://doi.org/10.3389/frwa.2021.772185

Florentine, C., Skidmore, M., Speece, M., Link, C., & Shaw, C. A. (2014). Geophysical analysis of transverse ridges and internal structure at Lone Peak Rock Glacier, Big Sky, Montana, USA. *Journal of Glaciology*, *60*(221), 453–462. https://doi.org/10.3189/2014JoG13J160

Head, J. W., Marchant, D. R., Dickson, J. L., Kress, A. M., & Baker, D. M. (2010). Northern mid-latitude glaciation in the Late Amazonian period of Mars: Criteria for the recognition of debris-covered glacier and valley glacier land system deposits. *Earth and Planetary Science Letters*, *294*(3), 306–320. https://doi.org/10.1016/j.epsl.2009.06.041

Heincke, B., Günther, T., Dalsegg, E., Rønning, J. S., Ganerød, G. V., & Elvebakk, H. (2010). Combined three-dimensional electric and seismic tomography study on the Åknes rockslide in western Norway. *Journal of Applied Geophysics*, *70*(4), 292–306. https://doi.org/10.1016/j.jappgeo.2009.12.004

Holt, J. W. (2021). Reflection and Refraction Active Seismic Acquisition on Sourdough Rock Glacier, McCarthy, Alaska [Dataset]. International Federation of Digital Seismograph Networks. https://doi.org/10.7914/SN/2E_2021

Holt, J. W., Safaeinili, A., Plaut, J. J., Head, J. W., Phillips, R. J., Seu, R., et al. (2008). Radar Sounding Evidence for Buried Glaciers in the Southern Mid-Latitudes of Mars. *Science*, *322*(5905), 1235–1238. https://doi.org/10.1126/science.1164246

Karslı, H., & Bayrak, Y. (2004). Using the Wiener–Levinson algorithm to suppress ground-roll. *Journal of Applied Geophysics*, *55*(3–4), 187–197. https://doi.org/10.1016/j.jappgeo.2003.11.003

Kawasaki, K., Osterkamp, T. E., Jurick, R. W., & Kienle, J. (1983). Gravity measurements in permafrost terrain containing massive ground ice. *Annals of Glaciology*, *4*, 133–140. https://doi.org/10.3189/S026030550000536X

Killingbeck, S. F., Livermore, P. W., Booth, A. D., & West, L. J. (2018). Multimodal layered transdimensional inversion of seismic dispersion curves with depth constraints. *Geochemistry, Geophysics, Geosystems*, *19*(12), 4957–4971. https://doi.org/10.1029/2018GC008000

Kingsley, S. A. (1986). Distributed fiber-optic sensors: An overview. In *Fiber optic and laser sensors III, 0566* (pp. 28–36). https://doi.org/10.1117/12.949760

Kohnen, H. (1974). The temperature dependence of seismic waves in ice. *Journal of Glaciology*, *13*(67), 144–147. https://doi.org/10.3189/S0022143000023467

Komatitsch, D. (1997). *Méthodes spectrales et éléments spectraux pour l'équation de l'élastodynamique 2D et 3D en milieu hétérogène*. Institut de Physique du Globe de Paris.

Komatitsch, D., Tromp, J., & Vilotte, J.-P. (1998). The spectral element method for elastic wave equations: Application to 2D and 3D. *Bulletin of the Seismological Society of America*, *88*(2), 368–392. https://doi.org/10.1785/bssa0880020368

Kuehn, T. (2023). Active seismic refraction, reflection and surface-wave exploration in debris-covered glacial environments, Sourdough and Malaspina Glaciers, Alaska [Dataset]. University of Arizona Research Data Repository. https://doi.org/10.25422/azu.data.19758499.v1

Langston, G., Bentley, L. R., Hayashi, M., McClymont, A., & Pidlisecky, A. (2011). Internal structure and hydrological functions of an alpine proglacial moraine. *Hydrological Processes*, *25*(19), 2967–2982. https://doi.org/10.1002/hyp.8144

LeBlanc, A. M., Fortier, R., Allard, M., Cosma, C., & Buteau, S. (2011). Seismic cone penetration test and seismic tomography in permafrost. *Canadian Geotechnical Journal*, *41*(5), 796–813. https://doi.org/10.1139/t04-026

Levy, J. S., Fassett, C. I., Head, J. W., Schwartz, C., & Watters, J. L. (2014). Sequestered glacial ice contribution to the global Martian water budget: Geometric constraints on the volume of remnant, midlatitude debris-covered glaciers. *Journal of Geophysical Research: Planets*, *119*(10), 2188–2196. https://doi.org/10.1002/2014JE004685

Maurer, H., & Hauck, C. (2007). Geophysical imaging of alpine rock glaciers. *Journal of Glaciology*, *53*(180), 110–120. https://doi.org/10.3189/172756507781833893

Meng, T., Petersen, E., & Holt, J. (2022). Rock glacier composition and structure from radio wave speed analysis with dipping reflector correction. *Journal of Glaciology*, *69*(275), 1–19. https://doi.org/10.1017/jog.2022.90

Merz, K., Maurer, H., Rabenstein, L., Buchli, T., Springman, S. M., & Zweifel, M. (2016). Multidisciplinary geophysical investigations over an alpine rock glacier. *Geophysics*, *81*(1), WA147–WA157. https://doi.org/10.1190/geo2015-0157.1

Monnier, S., & Kinnard, C. (2013). Internal structure and composition of a rock glacier in the Andes (upper Choapa valley, Chile) using borehole information and ground-penetrating radar. *Annals of Glaciology*, *54*(64), 61–72. https://doi.org/10.3189/2013AoG64A107

Musgrave, A. W. (Ed.). (1967). *Seismic refraction prospecting*. Society of Exploration Geophysicists. https://doi.org/10.1190/1.9781560802679

Musil, M., Maurer, H., Green, A. G., Horstmeyer, H., Nitsche, F. O., Mühll, D. V., & Springman, S. (2002). Shallow seismic surveying of an Alpine rock glacier. *Geophysics*, *67*(6), 1701–1710. https://doi.org/10.1190/1.1527071

Nicholson, L., & Benn, D. I. (2006). Calculating ice melt beneath a debris layer using meteorological data. *Journal of Glaciology*, *52*(178), 463–470. https://doi.org/10.3189/172756506781828584

Olafsdottir, E. A., Erlingsson, S., & Bessason, B. (2018). Tool for analysis of multichannel analysis of surface waves (MASW) field data and evaluation of shear wave velocity profiles of soils. *Canadian Geotechnical Journal*, *55*(2), 217–233. https://doi.org/10.1139/cgj-2016-0302

Östrem, G. (1959). Ice melting under a thin layer of moraine, and the existence of ice cores in moraine ridges. *Geografiska Annaler*, *41*(4), 228–230. https://doi.org/10.1080/20014422.1959.11907953

Park, C. B., Miller, R. D., & Miura, H. (2002). Optimum field parameters of an MASW survey (Vol. *6*).

Park, C. B., Miller, R. D., & Xia, J. (1999). Multichannel analysis of surface waves. *Geophysics*, *64*(3), 800–808. https://doi.org/10.1190/1.1444590

Park, C. B., Miller, R. D., Xia, J., & Ivanov, J. (2007). Multichannel analysis of surface waves (MASW)—Active and passive methods. *The Leading Edge*, *26*(1), 60–64. https://doi.org/10.1190/1.2431832

Paul, F., Huggel, C., & Kääb, A. (2004). Combining satellite multispectral image data and a digital elevation model for mapping debris-covered glaciers. *Remote Sensing of Environment*, *89*(4), 510–518. https://doi.org/10.1016/j.rse.2003.11.007

Pavoni, M., Boaga, J., Wagner, F. M., Bast, A., & Phillips, M. (2023). Characterization of rock glaciers environments combining structurally-coupled and petrophysically-coupled joint inversions of electrical resistivity and seismic refraction datasets. *Journal of Applied Geophysics*, *215*, 105097. https://doi.org/10.1016/j.jappgeo.2023.105097

Petersen, E. I., Holt, J. W., Stuurman, C. M., Levy, J. S., Nerozzi, S., Paine, J. G., et al. (2016). Sourdough Rock Glacier, Alaska: An analog to Martian debris-covered glaciers. In *47th lunar and planetary science conference* (Vol. 2).

Petersen, E. I., Levy, J. S., Holt, J. W., & Stuurman, C. M. (2020). New insights into ice accumulation at Galena Creek Rock Glacier from radar imaging of its internal structure. *Journal of Glaciology*, *66*(255), 1–10. https://doi.org/10.1017/jog.2019.67

Potter, N., Jr. (1972). Ice-cored rock glacier, Galena Creek, northern Absaroka Mountains, Wyoming. *GSA Bulletin*, *83*(10), 3025–3058. https://doi.org/10.1130/0016-7606(1972)83[3025:IRGGCN]2.0.CO;2

Press, F. (1966). Section 9: Seismic velocities. In *Geological society of America memoirs* (Vol. 97, pp. 195–218). Geological Society of America. https://doi.org/10.1130/MEM97-p195

Richart, F. E., Hall, J. R., & Woods, R. D. (1970). *Vibrations of soils and foundations*. Prentice-Hall, Inc.

Ronczka, M., Hellman, K., Günther, T., Wisén, R., & Dahlin, T. (2017). Electric resistivity and seismic refraction tomography: A challenging joint underwater survey at Äspö Hard Rock Laboratory. *Solid Earth*, *8*(3), 671–682. https://doi.org/10.5194/se-8-671-2017

Rowan, A. V., Egholm, D. L., Quincey, D. J., & Glasser, N. F. (2015). Modelling the feedbacks between mass balance, ice flow and debris transport to predict the response to climate change of debris-covered glaciers in the Himalaya. *Earth and Planetary Science Letters*, *430*, 427–438. https://doi.org/10.1016/j.epsl.2015.09.004

Rücker, C., Günther, T., & Wagner, F. M. (2017). pyGIMLi: An open-source library for modelling and inversion in geophysics. *Computers & Geosciences*, *109*, 106–123. https://doi.org/10.1016/j.cageo.2017.07.011

Scherler, D., Bookhagen, B., & Strecker, M. R. (2011). Spatially variable response of Himalayan glaciers to climate change affected by debris cover. *Nature Geoscience*, *4*(3), 156–159. https://doi.org/10.1038/ngeo1068

Sheriff, R. E., & Geldart, L. P. (1982). *Exploration seismology*. Cambridge University Press.

Shumskiy, P. A. (1960). Density of glacier ice. *Journal of Glaciology*, *3*(27), 568–573. https://doi.org/10.3189/S0022143000023686

Spikes, K. T., Tisato, N., Hess, T. E., & Holt, J. W. (2019). Comparison of geophone and surface-deployed distributed acoustic sensing seismic data. *Geophysics*, *84*(2), A25–A29. https://doi.org/10.1190/geo2018-0528.1

Steeples, D. W., Green, A. G., McEvilly, T. V., Miller, R. D., Doll, W. E., & Rector, J. W. (1997). A workshop examination of shallow seismic reflection surveying. *The Leading Edge*, *16*(11), 1641–1647. https://doi.org/10.1190/1.1437543

Steeples, D. W., & Miller, R. D. (1998). Avoiding pitfalls in shallow seismic reflection surveys. *Geophysics*, *63*(4), 1213–1224. https://doi.org/10.1190/1.1444422

Tsoflias, G. P., Ivanov, J., Anandakrishnan, S., & Miller, R. (2008). Use of Active Source Seismic Surface Waves in Glaciology. In *Symposium on the application of geophysics to engineering and environmental problems 2008* (pp. 1240–1243). https://doi.org/10.4133/1.2963234

Uyanık, O. (2011). The porosity of saturated shallow sediments from seismic compressional and shear wave velocities. *Journal of Applied Geophysics*, *73*(1), 16–24. https://doi.org/10.1016/j.jappgeo.2010.11.001

Wagner, F. M., Mollaret, C., Günther, T., Kemna, A., & Hauck, C. (2019). Quantitative imaging of water, ice and air in permafrost systems through petrophysical joint inversion of seismic refraction and electrical resistivity data. *Geophysical Journal International*, *219*(3), 1866–1875. https://doi.org/10.1093/gji/ggz402

Xie, Z., Komatitsch, D., Martin, R., & Matzen, R. (2014). Improved forward wave propagation and adjoint-based sensitivity kernel calculations using a numerically stable finite-element PML. *Geophysical Journal International*, *198*(3), 1714–1747. https://doi.org/10.1093/gji/ggu219

Yang, Z., Dutta, U., Dutta, U., Xu, G., Hazirbaba, K., & Marx, E. E. (2011). Numerical analysis of permafrost effects on the seismic site response. *Soil Dynamics and Earthquake Engineering*, *31*(3), 282–290. https://doi.org/10.1016/j.soildyn.2010.08.004

Yde, J. C., & Paasche, Ø. (2010). Reconstructing climate change: Not all glaciers suitable. *Eos, Transactions American Geophysical Union*, *91*(21), 189–190. https://doi.org/10.1029/2010EO210001

Yilmaz, Ö. (2001). *Seismic data analysis: Processing, inversion, and interpretation of seismic data*. Society of Exploration Geophysicists. https://doi.org/10.1190/1.9781560801580